ACS Sustainable Resource Management

pubs.acs.org/acssrm

Article

Toward Higher Resource Efficiency in Solid–Fluid Reactions: Dye Adsorption Study on the Planetary Rotating Bed Reactor

Christian von Heynitz,*,† Felix Bachmann,*,† Thomas F. Hofmann, and Karl Glas

Cite This: ACS Sustainable Resour. Manage. 2024, 1, 1238–1246

Read Online

ACCESS | Metrics & More | Article Recommendations | Supporting Information

ABSTRACT: Most circular processing pathways involve solid–fluid reactions, such as adsorption, catalysis, degradation, and extraction. The reaction-harboring plant technology is crucial to the performance and resource efficiency of these processes. Therefore, this study investigates the technoecological characteristics of the planetary rotating bed reactor (PRBR) as a novel approach to solid–fluid reactions. Given its relevance in wastewater treatment, the adsorption of methylene blue (MB) from aqueous solution onto powdered activated carbon (PAC) served as a model process. Semicontinuous kinetic experiments were performed in a 2 L laboratory-scale PRBR by varying the amount of PAC, the rotational motion pattern, and the speed level. DIY inline photometry and volume flow control enabled a constant vessel concentration of MB and thus the acquisition of comparable adsorption rates. Torque measurement delivered the mechanical power consumption and allowed calculation of the emission cost per adsorbate. The results revealed a significant superiority of the distinctive planetary motion compared to a static particle bed in terms of mass transfer and energy efficiency. The adsorption rate increased up to a factor of 10 with the same power input. Furthermore, an optimal chamber filling was observed, reflecting the interplay between the particle mobility and available adsorption sites.

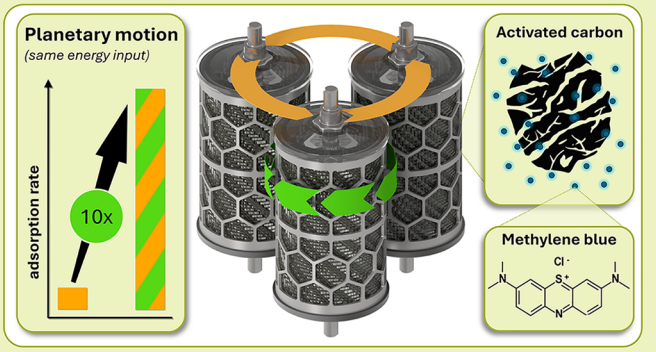

KEYWORDS: *solid–liquid, remediation, powdered activated carbon, water treatment, catalysis, mass transfer, heterogeneous reaction, reactor design*

INTRODUCTION

Many industrial processes involve heterogeneous reactions between dispersed particles and a liquid or gaseous phase. Following the green chemistry principles,[1] the intensification of such solid–fluid reactions plays a major role in the transformation to a circular economy. Examples of recent and future relevance are CO_2 capture[2] and water decontamination by adsorption.[3] In heterogeneous catalysis, the immobilization of enzymes[4] or inorganic catalysts[5] on solids is a key concept to facilitate their reuse.[1] The mechanoenzymatic degradation of lignocellulosic biomass[6] exemplifies a solid–liquid biorefinery process targeting a biobased economy. Solid–liquid extraction processes such as the recovery of critical minerals from electronic waste[7] are crucial for closing material cycles.

The key performance indicator of such processes is the reaction rate, governing process time, required plant size, resource demand, and thus the technoeconomic feasibility and environmental footprint. Naturally, the reaction rate of solid–fluid reactions depends on the mass transfer between the phases.[8] Addressing this dependence requires the development and use of appropriate reactor designs. This study therefore investigates the planetary rotating bed reactor (PRBR)[9] as a novel reactor design for solid–fluid reactions in circular economy processes.

Common reactor types for solid–fluid reactions are stirred-tank reactors (STRs), fluidized-bed reactors (FBRs), and packed-bed reactors (PBRs). Less common, but important to this study, is a group of reactors that we summarize as rotating compartment reactors (RCRs). By combining the advantages of these reactor types, the PRBR aims to overcome their limitations (Table 1).

The spinning basket reactor, a type of RCR, consists of an annular wire mesh basket, containing solid catalyst particles and rotating around its axis within a fluid vessel.[10] Like a radial flow pump, this rotation causes a centrifugal fluid flow through the particle packing, promoting solid–fluid interaction. Due to the axial re-entry of the flow into the basket (via top and bottom plates), a closed-flow circuit is established. Several

Received: March 6, 2024
Revised: April 26, 2024
Accepted: May 14, 2024
Published: May 24, 2024

Table 1. Properties of Common Reactor Designs and the PRBR Regarding Particle Compartmentalization, Prevention of Particle Phase Gradient Formation, and Enforcement of Interphase Motion in Solid−Fluid Reactions[a]

	particle compartmentalization	prevention of particle phase gradient	interphase motion
STR	-	+	-
FBR	-	0	0
PBR	+	-	0
RCR	+	0	0
PRBR	+	+	+

[a]The extent of the properties was marked semiquantitatively with the corresponding symbols.

similar reactor designs such as the Berty reactor, Carberry reactor, and Robinson−Mahoney reactor share the principle of a solid catalyst containing baskets.[11] Notably, these scale-down reactors were developed as a tool for the investigation of catalyst properties and reaction kinetics rather than industrial use.[12] The use of a rotating packed bed of catalyst to facilitate liquid−gas mass transfer was investigated in several studies over the past decades.[12,13] Recently, a rotating packed bed of Raschig rings in a cylindrical spinning basket reactor was as well proposed to enhance liquid−solid mass transfer,[13] combining principles of the PBR and RCR.

The PRBR adopts the principle of particle confining containers moving within a fluid. However, it comprises three cylindrical chambers that are arranged around the principal axis of a fluid vessel (Figure 1A).

Each chamber comprises a perforated lateral surface with a defined pore or mesh size, entrapping solid particles therein. The three-chamber assembly rotates around its center (vessel axis) to initiate a flow through the chambers, passing the perforated lateral walls. In this way, the entire assembly acts like a radial flow pump. Additionally, the chambers rotate around their cylindrical axes, relative and opposite to the rotation of the entire assembly. This planetary motion resembles the opposite rotations of Venus around its middle axis and around the Sun.

The superposition of rotations creates periodic accelerations experienced by the chamber, transmitted to the particles via contact forces (pushback effect).[14] The chambers are not entirely filled with particles. The resulting mobility of the particles allows for their circular agitation within the chambers (Figure 1B). This circulation can overcome the hydraulic barrier of static packed particle beds, as found in the RCR and PBR, and thus enhances the interaction with the passing fluid. In the PRBR, for demonstration and comparison, a static bed can be mimicked by eliminating the chambers' self-rotation (Figure 1C). The hydraulic resistance of static particle beds increases with decreasing size, decreasing shape stability, and increasing compression of the particles. However, the use of small particles (d < 100 μm) is required or favored in many processes due to their higher interaction surface. Low shape stability, on the other hand, is a common property of many materials relevant to the circular economy, such as biomass feedstocks.

Compartmentalization (Table 1) of the particles in the PBR, RCR, and PRBR eliminates the need for costly additional solid−liquid separation. Moreover, the planetary motion pattern of the PRBR allows the preprocess discharge of particles that are smaller than the aperture width of the perforated chamber walls, preventing the discharge of particles during a subsequent process step. The rotation of the RCR and even more the planetary motion of the PRBR allow for spin-drying of the particles to remove fluid residues. These aspects address two green chemistry principles: (1) the design for energy efficiency and waste prevention[1] by one-pot capabilities for simplification; (2) the prevention of hazardous substances[1]

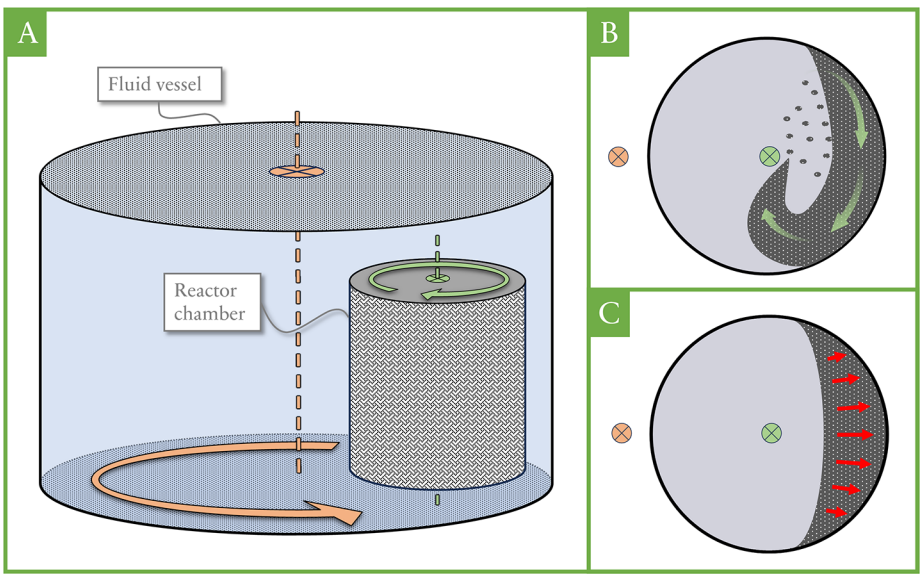

Figure 1. (A) Schematic representation of the PRBR with only one of the three reactor chambers shown. Rotation of the three-chamber assembly around the vessel axis (orange) and counterrotation of the chambers around the chamber axis (green) are indicated. (B) Reactor chamber in a sectioned top view representing the planetary motion pattern of the PRBR, resulting in circular agitation of the particles in the chamber, as indicated by green arrows. The positions of the vessel axis (orange) and chamber axis (green) are shown. (C) Same illustration logic as that for the planetary motion pattern but showing a static bed in the absence of chamber rotation. The time-constant centrifugal force is indicated by red arrows.

https://doi.org/10.1021/acssusresmgt.4c00089
ACS Sustainable Resour. Manage. 2024, 1, 1238−1246

by inline process analytics of the fluid phase without particle interference. Finally, compartmentalization prevents sedimentation of high-density particles (e.g., noble metals) and floating of low-density or hydrophobic particles.

In the PBR and RCR and to some extent in the FBR, the spatial distribution of phase interaction can be uneven. This results in gradients (Table 1) within the particle bed, e.g., in adsorbate loading. These inhomogeneities can, in turn, reduce the reaction rate and the efficiency of particle phase utilization. Such disadvantages can also result from channel formation within the particle bed. In contrast, the continuous spatial reorganization of the particles in the STR and PRBR prevents the formation of these gradients.

Interphase motion (Table 1) describes the flow velocity of the fluid relative to the particles and therefore promotes mass transfer through the boundary layer.[8] In the STR and FBR, small particles tend to move with the flow rather than being passed by it because there is no spatial fixation. In the FBR, this even leads to the risk of discharge by the flow. On the contrary, the PBR and RCR indeed provide such fixation by particle compartmentalization. However, the flow enforced through the packed particles is hydraulically limited by their aforementioned properties, such as size and stability. By continuous reorganization of the particles, the PRBR aims to break these hydraulic limitations. This ensures interphase motion, even for small and clogging-prone particles. The outlined disadvantages of packed beds inherent to the PBR and RCR are therefore avoided, while the benefits of compartmentalization are maintained.

An example for such challenging particles is powdered activated carbon (PAC), used as an adsorbent for the removal of dissolved contaminants from wastewater,[15,16] e.g., dyes from effluents in the textile industry. Inspired by this, the adsorption of methylene blue (MB) onto PAC was investigated in a 2 L laboratory-scale PRBR. Three parameters were varied: (1) the amount of PAC in the chambers, (2) the motion pattern of the PRBR, and (3) the speed level. The resulting adsorption rates as well as the corresponding mechanical power demands as an important part of plant operation costs were determined to investigate the kinetics and energy efficiency. Based on these quantities, the emission efficiency, expressed by CO_2 equivalents per adsorbed mass unit of dye, was calculated.

EXPERIMENTAL SECTION

Process Media. *Methylene Blue (MB) Solution.* MB in aqueous solution (pH 7, T = 20 °C) was used as the adsorbate. An MB stock solution (200 mg/L in ddH_2O) was diluted with potassium phosphate buffer (0.2 mM, pH 7, ddH_2O) to the target concentration. The required chemicals were purchased from Carl Roth GmbH & Co. KG (Karlsruhe, Germany).

Powdered Activated Carbon (PAC). PAC aktiwa-n from Hydrotec Handels GmbH (Berlin, Germany) with a declared cumulative volumetric particle size distribution of D_{10} = 3.35 μm, D_{50} = 25.90 μm, and D_{90} = 72.24 μm was used as the adsorbent. To obtain a defined size fraction and prevent particle wedging in the chamber mesh, the PAC was sieved to $36 < x < 63$ μm mesh size by dry-sieving twice with an AS 200 basic sieving machine from RETSCH GmbH (Haan, Germany) for 20 min at 90% amplitude, supported by rubber balls.

Testing Environment. Besides the laboratory-scale PRBR, the testing environment (Figure 2) includes a stirred feed tank (FT) with MB concentration c_0 and a collection tank (CT), an optical flow cell (OFC), and torque measurement equipment (T), integrated into the motors (M).

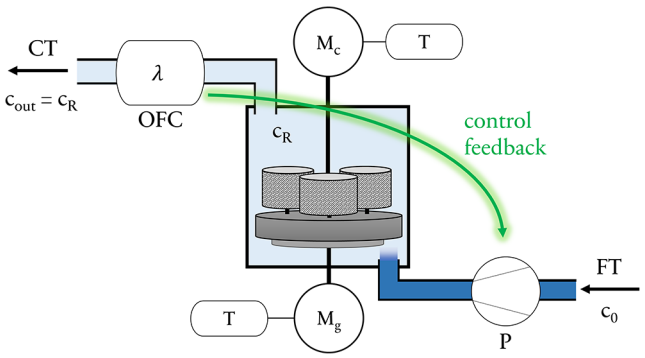

Figure 2. Sketch of the experimental setup including the three-chamber lab-scale PRBR with two motors M_c and M_g and torque measurement equipment T, as well as feed pump P and optical flow cell OFC. The MB solution with a concentration of c_0 is fed from a feed tank FT into the reactor vessel for adsorption. To maintain a constant MB concentration of c_R = 1 mg/L within the reactor vessel, the MB concentration is determined photometrically by the OFC and used as feedback for volume flow control of P.

During the experiments, the MB concentration in the reactor vessel (c_R) and thus that in the outflow (c_{out}) were kept constant by controlling the required flow rate of the feed pump (P). The MB concentration $c_R = c_{out}$ was measured with the OFC. This, in conjunction with the short measurement periods required, allowed determination of kinetics at a considerable distance from the adsorption equilibrium to ensure monolayer adsorption kinetics.

Laboratory-Scale PRBR. As shown in Figure 3, the laboratory-scale PRBR comprises a process platform (right) and an embeddable

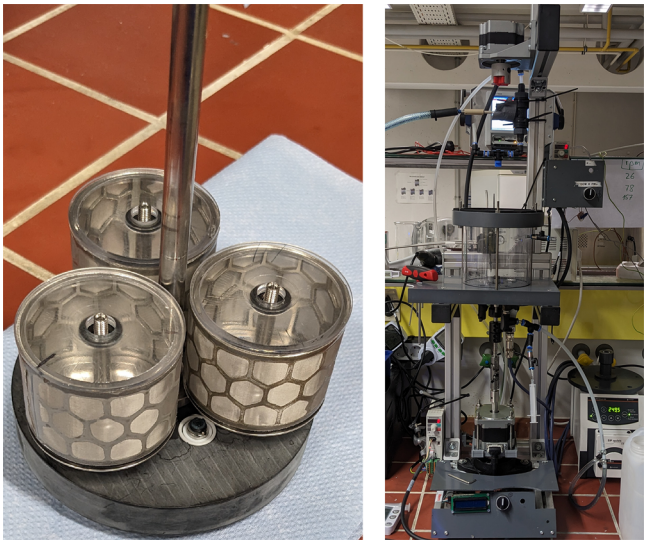

Figure 3. Photographs of the laboratory-scale PRBR. The three rotatably mounted reactor chambers along with the planetary carrier (black) form the reactor module (left), which can be mounted in the reactor vessel of the process platform (right).

reactor module (left) consisting of a planetary carrier (black) with three identical, rotationally arranged reactor chambers. It has been designed with standard engineering software tools and self-built with commercially available machine elements, materials, connections, and control technology. Each of the cylindrical chambers has an outer diameter of 56 mm, a height of 45 mm, and a net fill volume of 98 mL. The lateral surface is covered with 25 μm stainless-steel square mesh. The transparent lid plates are sealed with O-ring gaskets. The planetary gear drive (not shown) integrated in the carrier allows the chambers to rotate around their own axis while following the carrier's

https://doi.org/10.1021/acssusresmgt.4c00089
ACS Sustainable Resour. Manage. 2024, 1, 1238−1246

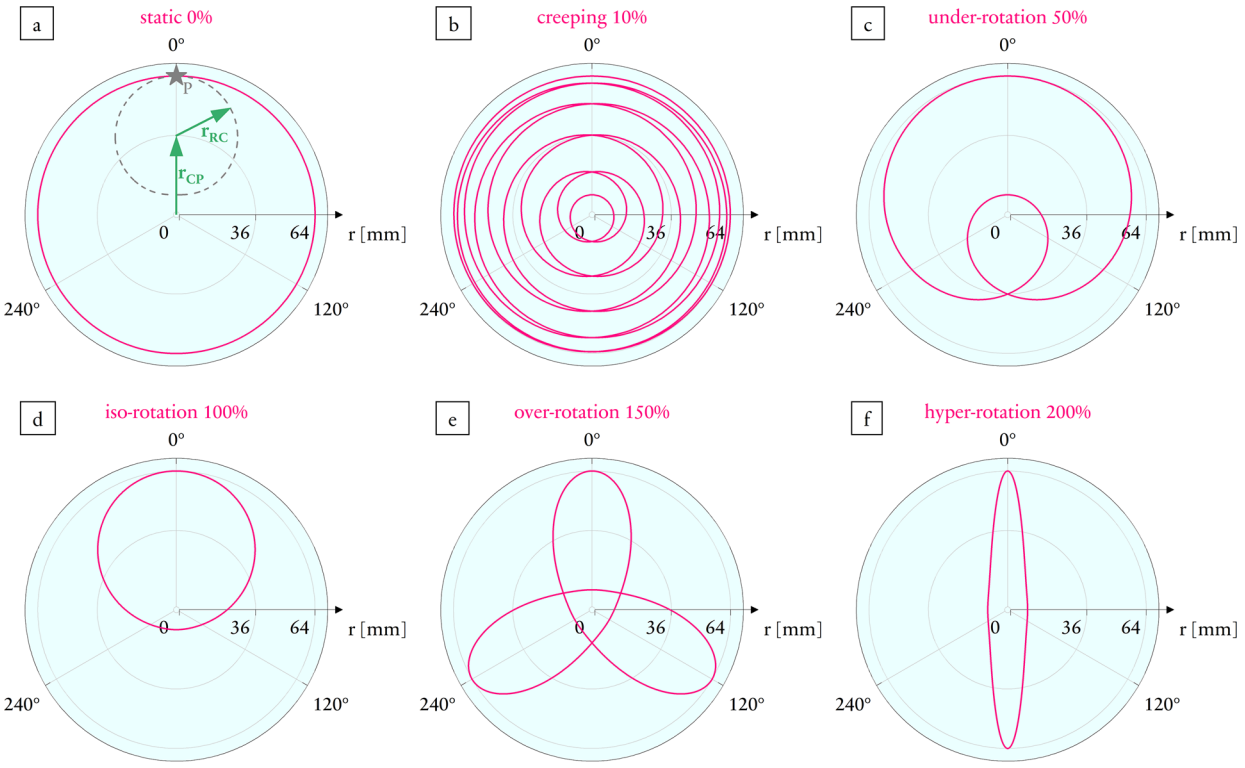

Figure 4. Top view of 2D trajectories of the virtual point P on the chamber wall for the six investigated motion patterns (a–f). The pattern names are inspired by the rotation rate of the chambers relative to the carrier together with the corresponding rpm ratio ϵ (%). (a) Contour of the reactor chamber with point P as well as the radii of the circular chamber path r_{CP} and reactor chamber r_{RC}. The curves are drawn until point P returns to its starting point $[r_{CP} + r_{RC}, 0°]$, resulting in a closed loop. As the selected rpm ratios are rational numbers, this corresponds to a finite number of chamber/carrier rotations. The curves differ in their length and curvature. For instance, in isorotation $\{\epsilon_{100}\}$, P describes a circle with a radius of 72 mm that is offset from the center. Due to the equally high counterrotation speed of the chamber and carrier, the orientation of the chamber relative to the vessel remains constant.

rotation.[14,17] The self-rotation is defined by the speed of the chambers relative to the carrier n_{RC}, whereas the carrier speed n_c is defined as absolute in the inertial system defined by the stationary vessel. The process platform holds the two drive trains, the cylindrical 2 L reactor vessel, and electrical and hydraulic ports. A drive shaft passing through the bottom plate of the vessel drives the planetary gear drive (n_g) to control the self-rotation of the chamber n_{RC}. Another drive shaft entering through the top plate of the vessel drives the carrier. The shafts are driven by two Oriental BLE2 AC brushless motors with respective Oriental BLE2 controllers (Oriental Motor Company, Ltd., Tokyo, Japan).

Inline Photometry. The MB concentration was measured using a self-made photospectrometric flow cell, comprising a fiber-optic cuvette holder FOFMS/M (Thorlabs GmbH, Bergkirchen, Germany) holding a modified 10 × 10 mm quartz glass cuvette. This modification features inflow and outflow ports manufactured by 3D printing (PLA). This allowed for a cost-effective solution based on the existing equipment and the technical conditions like flow rate, required optical path length, and mounting options. The flow cell was optically connected to a HL-2000-LL halogen lamp (Ocean Optics B.V., Duiven, The Netherlands) as a light source and a STS-VIS-L-25-400-SMA visible photospectrometer (Ocean Optics B.V., Duiven, The Netherlands) as a receiver. For these connections, two MHP200L0 fiber-optic cables (Thorlabs GmbH, Bergkirchen, Germany) were used.

The MB concentration was measured by reading the extinction at 665 nm (absorption maximum), while the extinction at 800 nm indicated turbidity to monitor the removal of fine dust from PAC. The measured values were transmitted to a PC connected to the spectrometer via USB using *MATLAB* (R2023b).

Electronic Torque Measurement. Shaft torques were measured by the BLE2 motor controller (Oriental Motor Company, Ltd., Tokyo, Japan) based on the electrical motor current.

Feed Pump. The flow rate was controlled using a Hei-FLOW Ultimate 600 peristaltic pump equipped with Tygon tubing of 2.5 mm wall thickness (Heidolph GmbH, Schwabach, Germany).

Altered Parameters. *PAC Mass (Chamber Filling).* The amounts of 5, 10, and 20 g of PAC per reactor chamber were employed. This corresponds to reactor chamber filling volumes of 18%, 36%, and 72%, respectively.

Motion Pattern (rpm Ratio). The rotational motion pattern of the PRBR is defined by the rpm ratio ϵ of the reactor chambers n_{RC} to the carriers' rotational speed n_c as per

$$\epsilon = \frac{n_{RC}}{n_c}\ (\%)$$

The rotation of the chambers at their rotational speed n_{RC} is defined relative to the carrier and is referred to as "chamber rotation" throughout this study.

The motion pattern can be illustrated by the 2D trajectory of a point P on the lateral chamber wall. It is described by a parametric curve providing the position of P in Cartesian $[(x_P, y_P)]$ and polar $[(R_P, \Phi_P)]$ coordinates with reference to the carrier rotational angle φ_c as the path parameter:

$$\vec{x}(\varphi_c) = \begin{bmatrix} x_P \\ y_P \end{bmatrix} = \begin{bmatrix} R_P \cos(\phi_P) \\ R_P \sin(\phi_P) \end{bmatrix} = r_{CP} \begin{bmatrix} \cos(\varphi_c) \\ \sin(\varphi_c) \end{bmatrix} + r_{RC} \begin{bmatrix} \cos[\varphi_c(\epsilon + 1)] \\ \sin[\varphi_c(\epsilon + 1)] \end{bmatrix}$$

https://doi.org/10.1021/acssusresmgt.4c00089
ACS Sustainable Resour. Manage. 2024, 1, 1238−1246

Table 2. Overview of All Rotational Speeds (in rpm) with Respect to the Speed Level and Motion Pattern[a]

		speed level (≙ carrier speed)					
		300 rpm		500 rpm		700 rpm	
motion pattern	rpm ratio ϵ (%)	n_{RC}	$n_g = n_{RC}^{abs}$	n_{RC}	$n_g = n_{RC}^{abs}$	n_{RC}	$n_g = n_{RC}^{abs}$
static mode	0	0	300	0	500	0	700
creeping	10	−30	270	−50	450	−70	630
underrotation	50	−150	150	−250	250	−350	350
isorotation	100	−300	0	−500	0	−700	0
overrotation	150	−450	−150	−750	−250	−1050	−350
hyperrotation	200	−600	−300	−1000	−500	−1400	−700

[a]This includes the reactor chamber speed n_{RC} as well as systematically equivalent absolute chamber speed n_{RC}^{abs}. The systematic equivalence of n_{RC}^{abs} and n_g is due to the operation of the planetary gear drive.[17] Although the chamber rotation is opposite to that of the carrier and therefore has a negative sign, its absolute rotation in space is positive for rpm ratios ϵ of <100%. Accordingly, the drives rotate in the same direction in these modes.

r_{CP} and r_{RC} denote the radii of the chambers' circular travel path (36 mm) and the reactor chamber itself (28 mm). Figure 4 shows the trajectories of the six motion patterns (rpm ratios, ϵ) investigated in this study.

The static mode with rpm ratio 0% (Figure 4a) is defined by a reactor chamber behaving as if it was fixed to the carrier, i.e., showing no chamber rotation. Therefore, the PAC particle bed is statically compressed by a constant centrifugal force resulting from the carrier rotation (see also Figure 1C). Accordingly, this mode serves as a reference mimicking conventional PBR and RCR. The other patterns (Figure 4b–f) are representatives of the distinctive planetary motion pattern.

Speed Level (Carrier rpm). To investigate the influence of the speed at which the six motion patterns traveled, three speed levels were defined. These refer to the carrier speed as the principal rotation and are set to 300, 500, and 700 rpm. Table 2 provides the speeds of the reactor chamber n_{RC}, defined as relative to the carrier rotation, and the absolute chamber speed n_{RC}^{abs} and gear drive shaft speed n_g, for all speed levels and respective motion patterns.

Outcome Metrics. *Adsorption Rate from Kinetic Study.* A full factorial kinetic study, based on the three altered parameters, resulted in a total of 54 setups. For each experiment, the reactor chambers were filled with the weighed PAC mass and sealed. After the reactor module was mounted within the process platform, the remaining PAC fine dust was washed out in isorotation $\{\epsilon_{100}\}$ at 700 rpm and a flow rate of 500 mL/min using 0.2 mM potassium phosphate buffer. The resulting grayish turbidity was measured in the flow cell and used to control the washing progress. The feed was then switched to the FT with an MB solution of c_0. The pump rpm was adjusted to the flow rate to ensure a constant reactor MB concentration of c_R = 1 mg/L.

A consistent MB concentration facilitated comparability while avoiding the interpretation risks of pseudokinetic models.[18] Due to the wide range of adsorption rates, not only the measured variable flow rate $\dot{V}$ but also the input concentration of MB c_0 (3, 5, 10, 15, and 20 mg/L) had to be varied to ensure c_R = 1 mg/L. To determine the adsorption rate $\dot{m}_{ad}$, the MB mass balance of the reaction vessel is used:

$$\dot{V}_{in}c_0 = \dot{V}_{out}c_{out} + \int_V \frac{\partial c_R(x_f)}{\partial t}\,dV + \dot{m}_{ad}$$

The input flow $\dot{V}_{in}$ and output flow $\dot{V}_{out}$ are equal and therefore correspond to $\dot{V}$. The constant concentration $\frac{\partial c_R(x_f)}{\partial t} = 0$ causes the volume integral over the vessel to be zero. For $\dot{m}_{ad}$, this results in

$$\dot{m}_{ad} = \dot{V}(c_0 - c_{out})$$

Mechanical Power and Emission Cost per Adsorbate (ECA). The process power demand is given by the two shaft power inputs of the carrier $P_{m,c}$ and chamber driving gear drive $P_{m,g}$. These result from the respective angular velocities ω and the measured torques T reduced by the vessel gasket friction T_0:

$$P_m = P_{m,c} + P_{m,g} = (T_c - T_{c,0})\omega_c + (T_g - T_{g,0})\omega_g$$

All setups (speed level and rpm ratio) were executed serially with a single PAC loading per PAC mass. Therefore, all speed levels from 100 to 800 rpm were determined in steps of 100, providing a more comprehensive view and increased error robustness. The three PAC masses, six rpm ratios, and eight speed levels led to a full factorial experiment with 144 setups. For better comparability, the tests were conducted with $\dot{V}$ = 0 mL/min. The generated power-rpm curves of the two drive trains were fitted with a cubic approach function $P_m(\omega_c) = \sum_{i=0}^{3} a_i\omega^i$ to increase the statistic robustness according to a turbulent flow regime. To relate the adsorption rates from the kinetic study to not only the power input but also the associated environmental impact, associated greenhouse gas emissions were considered. Addressing the green engineering principle of the design for separation[19] and its focus on minimizing resource footprint, CO_2 equivalents per adsorbed mass unit of adsorbate (MB) were calculated. Leaning on the carbon emission intensity per kilowatt-hour (CIPK; 251 g/kWh within the EU in 2022),[20] the ECA was defined as

$$\mathrm{ECA} = \frac{m_{CO2e}}{m_{ad}} = \frac{E_m\mathrm{CIPK}}{m_{ad}} = \frac{P_m\mathrm{CIPK}}{\dot{m}_{ad}}$$

RESULTS AND DISCUSSION

Adsorption Rate. Figure 5 shows the adsorption rate over the rpm ratio (motion pattern). The nine resulting curves are arranged in two ways: segregated by PAC mass (Figure 5a–c) and segregated by speed level (Figure 5d–f).

Higher speed levels lead to higher adsorption rates for all combinations of PAC mass and rpm ratio (Figure 5a–c). This can be explained by the associated higher centrifugal accelerations increasing the flow of liquid through the chambers, promoting mass transfer. Given a certain motion pattern/rpm ratio, the speed of the chamber rotation increases proportionally with the speed level, thereby enhancing circular agitation of the particle bed. This does not apply for the non-agitated particle bed in static mode $\{\epsilon_0\}$.

The overall higher adsorption rate of the planetary motion patterns ($\epsilon_{10} - \epsilon_{200}$) compared to static mode $\{\epsilon_0\}$ is clearly reflected by all curves (Figure 5). Even a slow chamber rotation (creeping $\{\epsilon_{10}\}$) leads to a significant increase by a factor of 4.5, appearing for 10 g of PAC and 500 rpm (Figure 5b). This illustrates that even slight particle motion can effectively mitigate the hydraulic limitations of a static particle bed. It is noticeable that for 5 g of PAC (Figure 5a) and all speed levels, as well as for 10 g of PAC for 500 and 700 rpm (Figure 5b), the adsorption rate reaches a maximum for overrotation $\{\epsilon_{150}\}$. As an example, this maximum amounts to

https://doi.org/10.1021/acssusresmgt.4c00089
ACS Sustainable Resour. Manage. 2024, 1, 1238−1246

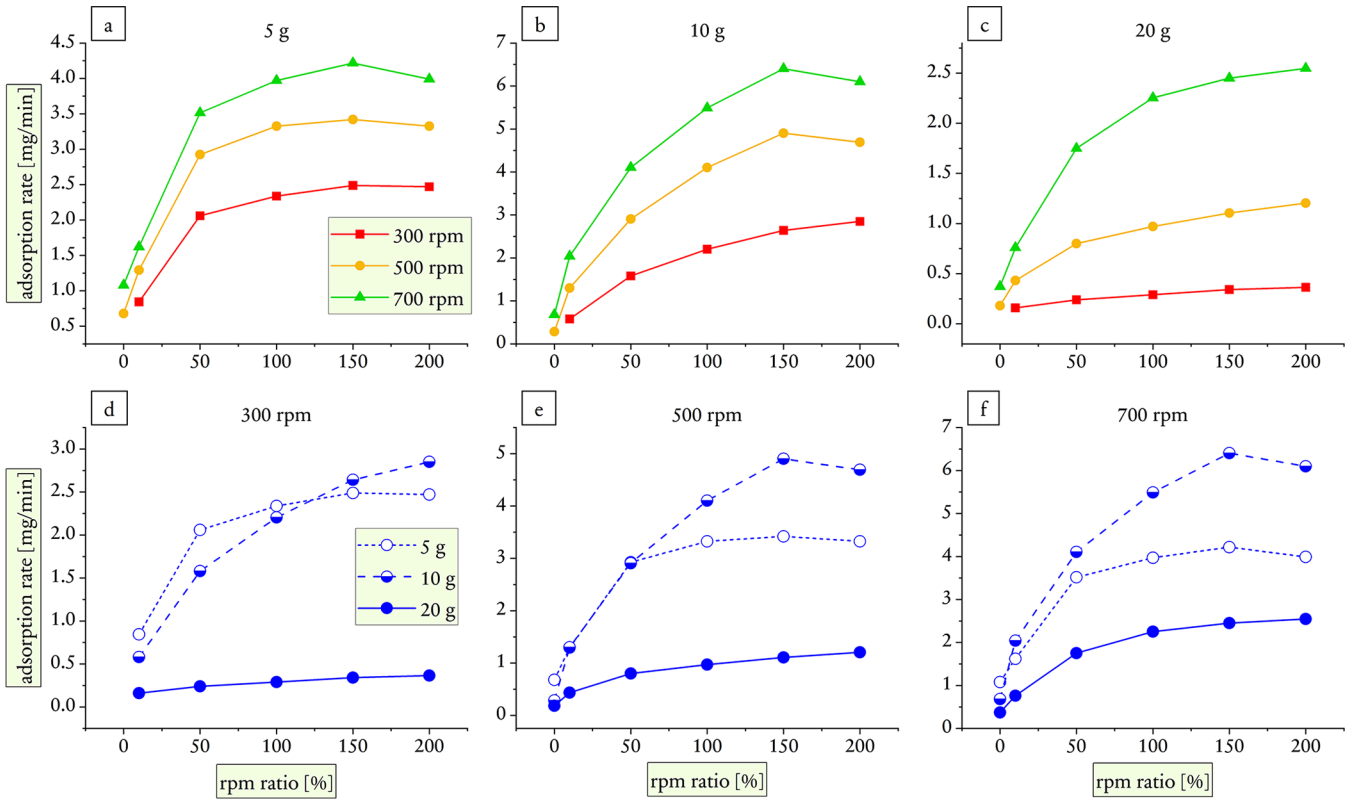

Figure 5. Adsorption rate over the rpm ratio (motion pattern), segregated by PAC mass (a–c) and speed level (d–f) with the same axis assignment. The missing data points for rpm ratio = 0 and 300 rpm could not be determined due to the flow rate limit of the used pump.

an increase by a factor of 17 compared to static mode $\{\epsilon_0\}$ for 10 g of PAC and 500 rpm (Figure 5b). In contrast, the curves for 20 g of PAC exhibit no maximum (Figure 5c), suggesting accessibility of the adsorption sites as rate-limiting step, caused by the limited mobility of the particles due to the high chamber filling of 72%. Thus, stronger agitation leads to increased accessibility and thus mass transfer in the boundary layer, facilitating occupation of the adsorption sites. Naturally, this positive effect on the adsorption rate is greater for larger PAC masses.

10 g PAC showed the highest adsorption rates, and 20 g PAC showed the lowest (Figure 5d–f). The better performance of 10 g of PAC is considerable for all planetary motion patterns with 700 rpm (Figure 5f), yet diminishing toward lower speed levels (Figure 5d,e). The lowest performance of 20 g of PAC is consistent, whereas the gap between 5 and 10 g of PAC shrinks toward lower speed levels. At 300 rpm, the adsorption rate with 10 g of PAC is still higher than that with 5 g of PAC for overrotation $\{\epsilon_{150}\}$, and for all lower rpm ratios, it is the other way around. Lower chamber fillings allow greater mobility and thus greater accessibility even at lower speed levels and rpm ratios. This outweighs the above-discussed exploitation of more PAC (with more adsorption sites) under these conditions.

To conclude, the adsorption rate can be well adjusted by the speed level. Compared to static mode $\{\epsilon_0\}$, the planetary motion patterns exhibit significantly superior adsorption rates, particularly overrotation $\{\epsilon_{150}\}$ and hyperrotation $\{\epsilon_{200}\}$. The findings suggest an optimal PAC mass, the value of which depends on the interplay between the motion pattern and speed level. Thus, there is a potential trade-off between the adsorption rate and the adsorption capacity.

Mechanical Power. Figure 6 shows the mechanical power consumption over the rpm ratio (motion pattern). The nine resulting curves are arranged in two ways: segregated by PAC mass (Figure 5a–c) and segregated by speed level (Figure 5d–f).

The curves reveal a general increase in power consumption with increasing rpm ratio and speed level (Figure 6a–c). While the power consumption increases by factors of 2–3 per speed level (Figure 6a–c), the increase from the thriftiest static mode $\{\epsilon_0\}$ to the most energy-intensive hyperrotation $\{\epsilon_{200}\}$ rarely exceeds factor 2 (Figure 6a–c).

The speed level is the more dominant factor because it has a twofold effect. (1) An increase in the speed level (=carrier speed) leads to an increase in the turbulent flow resistance of the entire reactor module (carrier and chambers). This generally includes the frictional forces in the shear layers between the chamber walls and the vessel wall (clearance of ca. 5 mm). The magnitude of these shear forces depends on the tangential speed of the chamber walls relative to the vessel wall and therefore not only on the carrier rotation alone but also on the reverse-directed chamber rotation. (2) By definition, for a given rpm ratio, the chamber speed changes proportionally with the carrier speed (=speed level) adjustments. This, in turn, produces another two opposing effects in terms of frictional forces. The counterrotation of the chambers relative to the carrier reduce their tangential speed relative to the vessel wall and thus the resulting frictional forces. However, at the same time, all frictional forces associated with chamber rotation as such increase. This includes friction in the bearings of the chambers, transmission losses in the planetary gears, and, above all, friction of the shear layers between the chambers themselves. For a given speed level, the significant

https://doi.org/10.1021/acssusresmgt.4c00089
ACS Sustainable Resour. Manage. 2024, 1, 1238–1246

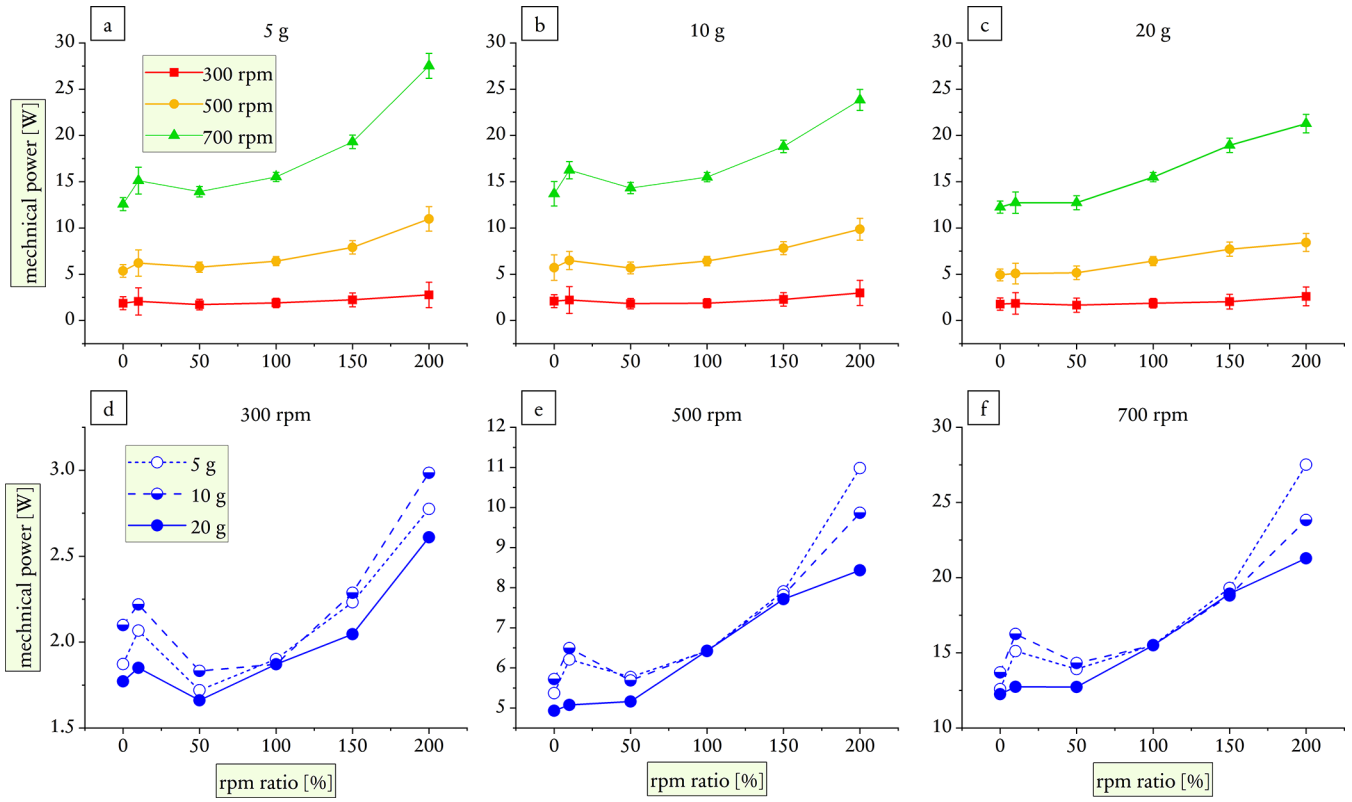

Figure 6. Mechanical power over the rpm ratio, segregated by PAC mass (a–c) and speed level (d–f) with the same axis assignment. Graphs a–c include 95% confidence intervals of the used regression for the underlying power-rpm curves to prove data consistency.

increase in power consumption with increasing rpm ratio shows that the frictional effects of chamber rotation increasingly outweigh the reduction in the tangential speed and thus vessel friction.

These considerations contribute to understanding the peaks in the power requirement for creeping $\{\epsilon_{10}\}$ with 5 and 10 g of PAC for all speed levels (Figure 6d–f) as well as for 300 rpm and 20 g of PAC. In static mode $\{\epsilon_0\}$, the aforementioned chamber counterrotation frictional forces do not occur, explaining the lower power requirement compared to creeping $\{\epsilon_{10}\}$. Toward higher rpm ratios, the lower tangential speed between the chambers and the vessel leads to lower shear frictions, resulting in a reduced power requirement.

The values for creeping $\{\epsilon_{10}\}$ and hyperrotation $\{\epsilon_{200}\}$ are accompanied by comparatively high confidence intervals. They express the uncertainty in the regression. With creeping $\{\epsilon_{10}\}$, periodic fluctuations in the torque of both motors were already noticeable during the measurements. These may have been caused by periodic flow phenomena and the speed controllers' effort to compensate for this. The fact that, in creeping $\{\epsilon_{10}\}$, the motors rotate in the same direction (Table 2) leads to an undefined load distribution on both motors, which further worsens this instability (like two persons trying to push a broken-down car with a defined share of pushing forces). The increased uncertainty for hyperrotation $\{\epsilon_{200}\}$ is probably caused by randomly occurring frictional effects, such as trapped air bubbles, which intensify with higher chamber speeds.

In general, the effect of the PAC mass on the power consumption is marginal; however, 5 and 10 g of PAC require slightly more power than 20 g under otherwise same conditions (Figure 6d–f). Less PAC corresponds to a lowered hydraulic barrier and therefore a higher flow rate. This increases the torque requirement, in line with the aforementioned analogies to a radial flow pump. Interestingly, in isorotation $\{\epsilon_{100}\}$, the change in power among the PAC masses is close to zero possibly because the gear drive shaft stands still ($\omega_g = 0 \rightarrow P_g = 0$), and thus only the carrier drive train rotates.

In summary, the planetary motion patterns lead to an up to 2.5-fold increase in power consumption compared to the static mode $\{\epsilon_0\}$ under otherwise the same conditions. The speed level has an even more significant effect, while the effect of the PAC mass is marginal. Further and more in-depth explanations of the fluid–mechanical interactions that cause the observed power characteristics can be revealed by numerical 3D models.

Energy Efficiency and Technoecological Evaluation. Figure 7 relates the adsorption rate to the mechanical power input, segregated by the PAC mass. This allows for a comparative assessment of both the energy efficiency and associated ECA. The planetary motion patterns show superior energy efficiency over the static mode $\{\epsilon_0\}$ for all PAC masses.

The ranking of the motion patterns regarding the energy efficiency is consistent across all PAC masses (Figure 6a–c): from low in static mode $\{\epsilon_0\}$ to significantly higher in creeping mode $\{\epsilon_{10}\}$ to exceptionally high in stronger planetary motion patterns. With 5 g of PAC, underrotation $\{\epsilon_{50}\}$ and hyperrotation $\{\epsilon_{200}\}$ show an almost congruent relationship between the adsorption rate and power input (Figure 6a). The same applies for the even more energy-efficient isorotation $\{\epsilon_{100}\}$ and overrotation $\{\epsilon_{150}\}$ (Figure 6a). Both examples illustrate how a higher adsorption rate (Figure 5a) might be nullified by a higher power requirement (Figure 6a) in terms of energy efficiency. With 10 g of PAC, isorotation $\{\epsilon_{100}\}$ and hyperrotation $\{\epsilon_{200}\}$ show a congruent relationship, while overrotation $\{\epsilon_{150}\}$ is the most energy efficient (Figure 6b).

https://doi.org/10.1021/acssusresmgt.4c00089
ACS Sustainable Resour. Manage. 2024, 1, 1238–1246

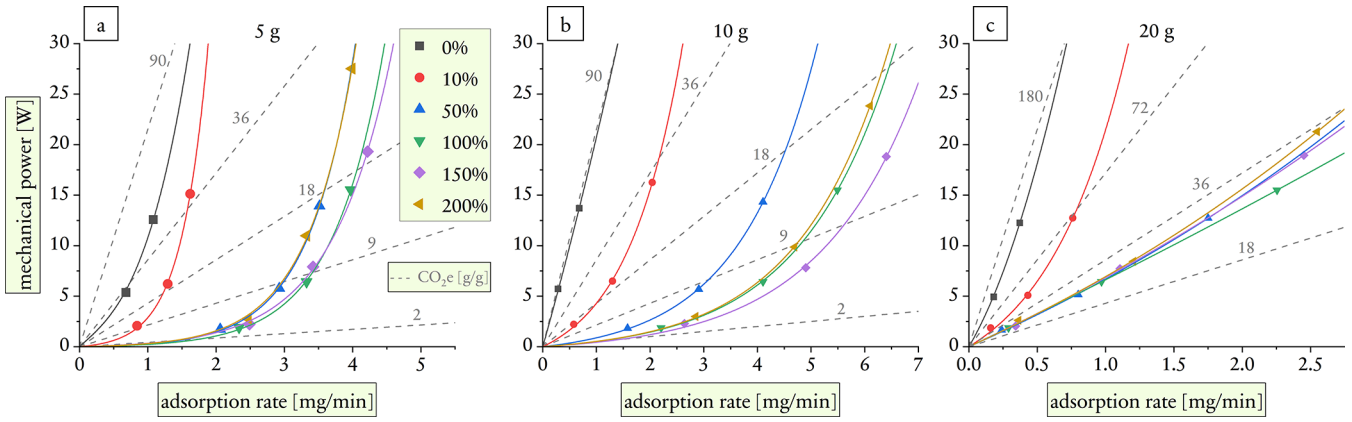

Figure 7. Mechanical power over the adsorption rate for the three PAC masses, showing the rpm ratio (motion pattern) as a set of points. For a better illustration, the curves represent a data fit with a pragmatically selected exponential function $P_m = C_1[1 - \exp(-C_2\dot{m}_{ad})]$. The dashed lines indicate the attributable amount of CO_2 equivalent per adsorbed mass unit of dye (ECA = emission cost per adsorbate).

With 20 g of PAC, the curves are almost the same for all planetary motion patterns except creeping $\{\epsilon_{10}\}$ (Figure 6c).

Calculation of the ECA considers the carbon emissions associated with the mechanical power requirement based on the CIPK. The ECA for 20 g of PAC is overall higher than for 5 and 10 g (Figure 7) because the adsorption rate is lower than with other PAC masses while barely differing in the power requirement. Notably, for all planetary motion patterns except creeping $\{\epsilon_{10}\}$, the ECA with 10 g of PAC is lower than that with 5 g of PAC, given the same adsorption performance. Consequently, with respect to ECA, 10 g of PAC emerges as superior.

For 10 g of PAC, static mode $\{\epsilon_0\}$ follows the ECA isoline of 90 g/g (Figure 7b). Given a mechanical power input of 15 W, the use of the most energy-efficient overrotation $\{\epsilon_{150}\}$ results in an ECA of 9 g/g, which corresponds to a 10-fold decrease compared to static mode $\{\epsilon_0\}$ (Figure 7b).

The curvatures decrease toward higher PAC masses (Figure 7a–c), reaching almost linear character with 20 g of PAC (Figure 7c). Regardless of the planetary motion pattern (except creeping $\{\epsilon_{10}\}$), the adsorption rate almost proportionally increases with the power input, with a nearly constant ECA of ∼8 g/g (Figure 7c). This resonates the accessibility aspects explained in the context of the determined adsorption rates.

All things considered, the planetary motion pattern turned out to be superior to a static particle bed, both with an exclusive view on the adsorption rate and with regard to the energy efficiency and resulting ECA. While the inferiority of 20 g of PAC mass already turned out in terms of the adsorption rate, the ranking between 5 and 10 g remained ambiguous. By taking into account the energy efficiency and resulting ECA, the optimum at 10 g was clearly revealed. The use of PAC in this study exemplifies both a widespread adsorbent and a particle size range of industrially relevant powdery substances that are prone to clogging. The suitability of the PRBR's inherent planetary motion patterns by increasing the hydraulic accessibility of such particles was shown. Thus, the assumed superiority of the PRBR over existing reactor designs with static particle beds such as the RCR was confirmed.

CONCLUSION

The study demonstrates the technoecological potential of the PRBR for solid–fluid reactions in the circular economy. The distinctive planetary motion pattern significantly accelerated mass transfer and showed superior emission efficiency, underlining the limitations of existing reactor designs with a static particle bed. Furthermore, it was shown that increasing the reaction rate by increasing chamber filling is limited. The real-time adjustability of kinetics by the speed level allows effective and adaptive process control, also with regard to process safety. The findings of this investigation together with the suitability for sustainability-promoting one-pot operations qualify the PRBR for a variety of industrial applications as an economical and environmentally friendly process platform. The PRBR can be integrated into industrial plants via standard connections and in compliance with the space and safety requirements common to vessel-type reactors. The potential also extends to the usability as a test platform for the development of new sustainable materials, e.g., biobased adsorbents, providing well-defined experimental conditions and analytical accessibility.

Further experimental and numerical investigations can provide a deeper understanding of the PRBR, in particular, its fluid mechanical phenomena and their relation to mass transfer and energy consumption. Beyond that, further development should target application transfer and thus optimization and upscaling of the plant design toward the needs of a circular economy.

ASSOCIATED CONTENT

Supporting Information

The Supporting Information is available free of charge at https://pubs.acs.org/doi/10.1021/acssusresmgt.4c00089.

Characterization of the PAC (Fourier transform infrared spectrum, physical properties, pore characterization, and particle size distribution) and information on the adsorption mechanisms and adsorption process control (PDF)

AUTHOR INFORMATION

Corresponding Authors

Christian von Heynitz − *Food Chemistry and Molecular Sensory Science, School of Life Sciences, Technical University of Munich, 85354 Freising, Germany*; Email: c.heynitz@tum.de

https://doi.org/10.1021/acssusresmgt.4c00089
ACS Sustainable Resour. Manage. 2024, 1, 1238–1246

Felix Bachmann − *Fungal Biotechnology in Wood Science, School of Life Sciences, Technical University of Munich, 85354 Freising, Germany;* orcid.org/0009-0006-2822-8252; Email: f.bachmann@tum.de

Authors

Thomas F. Hofmann − *Food Chemistry and Molecular Sensory Science, School of Life Sciences, Technical University of Munich, 85354 Freising, Germany;* orcid.org/0000-0003-4057-7165

Karl Glas − *Food Chemistry and Molecular Sensory Science, School of Life Sciences, Technical University of Munich, 85354 Freising, Germany*

Complete contact information is available at: https://pubs.acs.org/10.1021/acssusresmgt.4c00089

Author Contributions

†C.v.H. and F.B. contributed equally to this paper.

Author Contributions

C.v.H.: conceptualization, project administration, investigation, visualization, and writing. F.B.: methodology, investigation, visualization, and writing. T.F.H.: funding acquisition and writing—review and editing. K.G.: supervision, formal analysis, and validation.

Notes

The authors declare the following competing financial interest(s): C.v.H. is the inventor of Patent EP3669976B1 issued to the Technical University of Munich.

■ ACKNOWLEDGMENTS

This work was supported by the Bavarian Ministry of Economic Affairs Regional Development and Energy (StMWi) via the BayVFP program (Grant LSB-2011-0015).

■ REFERENCES

(1) Sheldon, R. A. Metrics of Green Chemistry and Sustainability: Past, Present, and Future. *ACS Sustainable Chem. Eng.* **2018**, *6* (1), 32−48.

(2) Dhoke, C.; Zaabout, A.; Cloete, S.; Amini, S. Review on Reactor Configurations for Adsorption-Based CO 2 Capture. *Ind. Eng. Chem. Res.* **2021**, *60* (10), 3779−3798.

(3) Vievard, J.; Alem, A.; Pantet, A.; Ahfir, N.-D.; Arellano-Sánchez, M. G.; Devouge-Boyer, C.; Mignot, M. Bio-Based Adsorption as Ecofriendly Method for Wastewater Decontamination: A Review. *Toxics* **2023**, *11* (5), 404.

(4) Sheldon, R. A.; Basso, A.; Brady, D. New frontiers in enzyme immobilisation: robust biocatalysts for a circular bio-based economy. *Chem. Soc. Rev.* **2021**, *50*, 5850.

(5) Wang, Y.; Shi, D.; Tao, S.; Song, W.; Wang, H.; Wang, X.; Li, G.; Qiu, J.; Ji, M. A General, Green Chemistry Approach for Immobilization of Inorganic Catalysts in Monolithic Porous Flow-Reactors. *ACS Sustainable Chem. Eng.* **2016**, *4* (3), 1602−1610.

(6) Xu, W.; Zhou, C.; Hu, K.; Yang, J.; Su, W.; Qiao, P. Novel Mechanoenzymatic Strategy for Lignin Depolymerization. *Ind. Eng. Chem. Res.* **2023**, *62* (46), 19448−19458.

(7) Sun, Z.; Cao, H.; Xiao, Y.; Sietsma, J.; Jin, W.; Agterhuis, H.; Yang, Y. Toward Sustainability for Recovery of Critical Metals from Electronic Waste: The Hydrochemistry Processes. *ACS Sustainable Chem. Eng.* **2017**, *5* (1), 21−40.

(8) Inglezakis, V. J.; Poulopoulos, S. G. Heterogeneous Processes and Reactor Analysis. In *Adsorption, Ion Exchange and Catalysis: Design of Operations and Environmental Applications*; Inglezakis, V. J., Poulopoulos, S. G., Eds.; Elsevier, 2006; pp 57−242. DOI: 10.1016/B978-044452783-7/50003-3.

(9) von Heynitz, C. Apparatus and method for promoting reaction in fluid media. European Patent 18215196.9.

(10) Myers, E. C.; Robinson, K. K. Multiphase Kinetic Studies with a Spinning Basket Reactor. In *Chemical Reaction Engineering—Houston*; ACS Symposium Series; Weekman, V. W., Luss, D., Eds.;American Chemical Society, 1978; pp 447−458. DOI: 10.1021/bk-1978-0065.ch037.

(11) Ountaksinkul, K.; Sripinun, S.; Bumphenkiattikul, P.; Vongachariya, A.; Praserthdam, P.; Assabumrungrat, S. A Review of Packed Bed Reactor and Gradient-less Recycle Reactor for Determination of Intrinsic Reaction Kinetics. *EJ.* **2022**, *26* (12), 17−42.

(12) Visscher, F.; van der Schaaf, J.; Nijhuis, T. A.; Schouten, J. C. Rotating reactors - A review. *Chemical Engineering Research and Design* **2013**, *91* (10), 1923−1940.

(13) Soliman, M. S.; Nosier, S. A.; Hussein, M.; Abdel-Aziz, M. H.; Sedahmed, G. H.; El-Naggar, M. A. Mass Transfer Behavior of a Rotating Packed Bed of Raschig Rings Suitable for Wastewater Treatment. *Chem. Eng. & Technol.* **2023**, *46* (8), 1679−1688.

(14) von Heynitz, C.; Stecker, M.; Hofmann, T.; Glas, K. A Novel Dry Hopping Technology: Kinematic Modelling of a Planetary Rotating Bed Reactor. *BrewingScience* **2020**, *73* (3), 68−76.

(15) Gong, Y.; Liu, F.; Liu, H.; Zhao, H.; Zhu, Y.; Han, Q.; Zhou, J.; Jiang, T.; Li, S. Environment-Energy-Economy Analysis and Related Technical Transition Strategies for Spent Activated Carbon Regeneration in China. *ACS Sustainable Chem. Eng.* **2022**, *10* (35), 11512−11523.

(16) Hwang, S. Y.; Lee, G. B.; Kim, J. H.; Hong, B. U.; Park, J. E. Pre-Treatment Methods for Regeneration of Spent Activated Carbon. *Molecules (Basel, Switzerland)* **2020**, *25* (19), 4561.

(17) von Heynitz, C.; Ohlmann, K.; Schmieder, B.; Hofmann, T.; Glas, K. Ultrafast extraction of cold brew coffee in a planetary rotating bed reactor: A kinetic study on the pushback effect. *J. Food Process Engineering* **2023**, e14473.

(18) Mudhoo, A.; Pittman, C. U. Adsorption data modeling and analysis under scrutiny: A clarion call to redress recently found troubling flaws. *Chemical Engineering Research and Design* **2023**, *192*, 371−388.

(19) Anastas, P. T.; Zimmerman, J. B. Design through the 12 principles of green engineering. *Environ. Sci. Technol.* **2003**, *37* (5), 94A−101A.

(20) Greenhouse gas emission intensity of electricity generation. https://www.eea.europa.eu/data-and-maps/daviz/co2-emission-intensity-14/#tab-chart_7 (accessed 2024-01-30).